Bernhard Stiehl
Propulsion and Energy Research Laboratory,
Center for Advanced Turbomachinery & Energy Research,
Department of Mechanical and Aerospace Engineering,
University of Central Florida,
4000 Central Florida Blvd.,
Orlando, FL 32816
e-mail: bernhard.stiehl@knights.ucf.edu

Michelle Otero
Propulsion and Energy Research Laboratory,
Center for Advanced Turbomachinery & Energy Research,
Department of Mechanical and Aerospace Engineering,
University of Central Florida,
4000 Central Florida Blvd.,
Orlando, FL 32816
e-mail: michelleotero@knights.ucf.edu

Tommy Genova
Propulsion and Energy Research Laboratory,
Center for Advanced Turbomachinery & Energy Research,
Department of Mechanical and Aerospace Engineering,
University of Central Florida,
4000 Central Florida Blvd.,
Orlando, FL 32816
e-mail: tommy.genova@knights.ucf.edu

Scott Martin
Embry-Riddle Aeronautical University,
600 S. Clyde Morris Blvd.,
Daytona Beach, FL 32114
e-mail: martis38@erau.edu

Kareem Ahmed
Propulsion and Energy Research Laboratory,
Center for Advanced Turbomachinery & Energy Research,
Department of Mechanical and Aerospace Engineering,
University of Central Florida,
4000 Central Florida Blvd.,
Orlando, FL 32816
e-mail: kareem.ahmed@ucf.edu

The Effect of Pressure on NO_x Entitlement and Reaction Timescales in a Premixed Axial Jet-In-Crossflow

This paper investigates the pressure dependency of a lean premixed jet injected into a lean vitiated crossflow with an experimentally verified detailed chemistry computational fluid dynamics (CFD) model and 53 species considered. Experimental data were taken in an axially staged combustor with an optically accessible test section, allowing the use of particle image velocimetry (PIV) and CH chemiluminescence techniques as well as point measurement of species concentration, temperature, and pressure. The experimental data cases at one, three, and five atmospheres were selected to describe the flame stabilization dependency on pressure and gain the required knowledge for an extrapolation to engine condition. Simulated exit nitrogen oxide levels were validated with experimental emission data, and a global emission trend for the NO reduction at elevated pressure and constant turbine inlet temperature level was defined. The nitrogen oxide benefit at elevated operating pressure was justified with the significantly smaller flame surface area: the analysis of the simulated spanwise and top-view profiles showed a relatively short receded core flame with nitrogen oxide production in the center at high pressure relative to a longer and larger shear layer flame at atmospheric condition that produced NO toward the inner and outer side of the flame. Decomposition of the Damköhler number revealed the strong influence of the reaction timescales with higher reaction rates at elevated pressure, along with a moderate influence of the turbulent timescales, showing higher turbulence intensity in the lee-side recirculation zone at lower pressure.* [DOI: 10.1115/1.4049609]

Keywords: reacting jet-in crossflow, axial fuel staging, axial-staged combustion, high-pressure, gas turbine combustor, NO_x emission, air emissions from fossil fuel combustion, energy conversion systems, fuel combustion

1 Introduction and Objectives

The present work investigates the influence of pressure on the reaction timescales and NO_x emission of a premixed jet in vitiated crossflow. The present study attempts to fill a gap about axial-staged combustor knowledge since a quantitative statement about the influence of pressure on NO_x emission has not been made in the open literature. The outcomes could be of high interest to further understand how applicable the data of flames at feasible laboratory pressure levels between 1 atm and 5 atm would be for burners at pressure levels 20–30 atm applied industrially. Patents in the field of axial-staged gas turbine combustion are owned by the OEMs Siemens [1,2] and GE [3,4].

On the experimental side, recent studies by Elkady et al. [5] investigated a perfectly premixed research burner operated at high-pressure levels between 8 atm and 16 atm. It was concluded that a pressure dependency of NO_x emission $X_{NO} \sim p^{const}$ can be formulated, but the constant would be temperature dependent. Higher pressure was shown to reduce both main stage burner NO_x and CO emission levels experimentally [5] with a pressure dependency in the range of $p^{0.5}$ for the main stage burner. Research by Gollahalli and Pardiwalla [6] focused on the influence of jet shape on the emission profiles of turbulent propane jet flames in crossflow. Experiments were conducted in a wind tunnel with an optically accessible test section attached. The upper and lower operating limits were screened by variation of the jet velocity. Lower CO

Contributed by the Advanced Energy Systems Division of ASME for publication in the Journal of Energy Resources Technology. Manuscript received November 13, 2020; final manuscript received January 4, 2021; published online February 19, 2021. Assoc. Editor: Ashwani K. Gupta.

emission and higher NO emission levels were the result of using elliptic jets relative to circular shaped jets [6]. A novel approach to obtain more reliable experimental NO_x emission monitoring was suggested by Al-Malak et al. [7], describing a soft emission analyzer that utilizes an artificial neural network. Blowout limits of a methane jet diffusion flame surrounded by smaller fuel-flex jet pilot flames and air co-flow were studied experimentally by Kibrya and Karim [8]. The blowout limit was extended by increasing the pilot jet flow, allowing enhanced entrainment and higher thermal contribution of the side jets [8]. Flame hysteresis effects of methane jet flames with variable air co-flow were studied experimentally by Moore et al. [9] to determine characteristics of the instantaneous turbulent flame liftoff relative to the fuel velocity. Critical operating parameters of lean partially premixed methane–air turbulent combustion were investigated experimentally by Askari et al. [10] in a constant volume combustion chamber and visualized with a Schlieren shadowgraph. The effect of hydrogen enrichment, equivalence ratio, diluent addition, variation of injection pressure, chamber pressure, temperature, and turbulence intensity (TI) were investigated. The addition of hydrogen was reported to be the critical parameter, allowing to improve the lean-burn limit of CH_4/air, improving peak p and T, and decreasing the duration of combustion cycles [10]. The utilization of process synergies and the integration of gasification into a combined cycle heavy-duty gas turbine system were studied experimentally and numerically by Liu et al. [11]. Required adaptations of conventional combustors to allow operation with syngas include the combustor head and nozzle arrangements. Numerical results were verified with experimental data, and a design was proposed for the mid- and high-pressure range.

Recent modeling efforts include a numerical large eddy simulation (LES) investigation with *STAR-CCM+* by Elgammal and Amano [12] on the thermal uniformity and pressure drop of jet-in-crossflow (JIC) mixing in a central swirler with staggered holes and various designs were able to document the axial and radial profiles with increased fidelity. The effects of distributed methane combustion on the temperature profile and thermal NO_x emission profile were investigated experimentally and numerically by Khalil et al. [13]. The distribution profiles were adjusted with a swirl field and variation of the CH_4/air premix state under lean conditions. Outcomes improved the pattern factor and achieved CO and NO_x emission levels in the low ppm range [13]. In a subsequent study by Khalil and Gupta [14], the influence of premixed fuel/air dual injection in the swirl field was documented and found to further reduce emissions relative to the single injection pattern studied by Khalil et al. [13]. A non-premixed turbulent jet flame (Sandia Flame D) was simulated with an experimentally verified LES by Safari and Sheikhi [15] to determine process irreversibilities and amount of entropy generation. Further numerical investigations by Deng et al. [16] covered the impact of nozzle configuration, such as the number and pattern of nozzles, the use of premixed and non-premixed nozzles, and jet velocity by applying moderate or intense low-oxygen dilution (MILD) principles to an F class gas turbine combustor. Simulation at industrially relevant condition $p =$ 16.3 bar, air temperature of 723 K, and a lean equivalence ratio of 0.625 suggested a number of 12 nozzles and jet velocity 110 m/s to be the optimal [16]. Simulations of an industrial gas turbine combustor were performed by Emami et al. [17] with gaseous CH_4 fuel under variation of the air flow distribution, recirculation, and dilution characteristics to optimize for CO and NO_x emission. Thermal NO_x and prompt NO_x formation mechanisms were considered, and the results emphasized the strong dependency of thermal NO_x levels on the local firing temperature and amount of air dilution [17].

Studies by Saini et al. [18] and Fleck et al. [19] investigated the effect of pressure on hydrogen enriched natural gas jet flames in crossflow at pressure levels 10 bar and 15 bar to determine the axial flame stabilization mechanism. Earlier studies [20,21] included qualitative emissions data under variation of the axial equivalence ratio and axial fuel split for axial-staged combustors and reheat combustors, but a trend of emission variation with pressure was not highlighted. A different experimental axial-staged combustion facility operating with a 0.8 mm methane jet in vitiated hot crossflow at pressure levels between 5 bar and 8 bar was investigated by Prathap et al. [22]. Emission measurements were taken, and axial NO_x addition with respect to the axial temperature rise was plotted at three pressure levels. However, a clear trend about the influence of pressure has not been determined, which could be justified with the pressure being varied between relatively high levels. The present study varies pressure level between 1 atm and 5 atm both experimentally and numerically. To extend the current knowledge to an axial combustion stage and isolate the known temperature dependency to a large extent, a constant centerline turbine inlet temperature level was targeted in this study and the mass flows scaled accordingly to account for the variation of pressure level. A trend was determined, and further understanding was sought with a time scale analysis. Critical relation to model a combustion process is the turbulent Damköhler number Da, defined as the ratio between the turbulent (= mixing) time scale and the chemical time scale (Eq. (1)):

$$\mathrm{Da} = \frac{\tau_{mix}}{\tau_{chem}} \tag{1}$$

τ_{mix} characterizes the local mixing time scale of the system as predefined in STAR-CCM+ [23] according to Eq. (2):

$$\tau_{mix} = (\beta^* \times \omega)^{-1} \tag{2}$$

with β^* being a model constant defined at 0.09 and ω being the specific dissipation rate. τ_{chem} was defined as a custom function based on local CO_2 properties according to the STAR-CCM+ Steve Portal (Eq. (3)), an article based on [24,25]

$$\begin{aligned}\tau_{chem} = [&(\varepsilon + \$\text{production rate CO}_2) \\ &\times (\varepsilon + \$\text{molecular weight CO}_2)^{-1} \\ &\times (\varepsilon + \$\text{molar concentration CO}_2)^{-1}]^{-1}\end{aligned} \tag{3}$$

τ_{chem} depends on the local CO_2 production rate, CO_2 molecular weight, local CO_2 molar concentration, and a very small number ε to avoid definition errors (1×10^{-12}). The Damköhler number is used in this study to characterize the variation of the flame type depending on the system pressure. τ_{mix} is a moderate function of pressure, meanwhile τ_{chem} was shown to be strongly pressure dependent. A chemical activity profile for a one-dimensional (1D) premixed laminar flame combustor and 250 dynamic grid points is shown in Fig. 1. The significant differences of maximum heat release levels as well as streamwise length of heat release indicate the necessity for a three-dimensional (3D) analysis for the relatively complex jet-in-crossflow field. The second objective of this paper was hereof defined to investigate the transition between shear

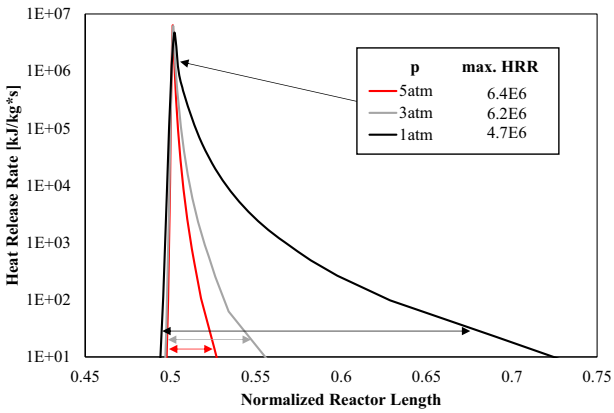

Fig. 1 Chemical heat release of a 1D premixed laminar reactor simulated with dynamic grid points

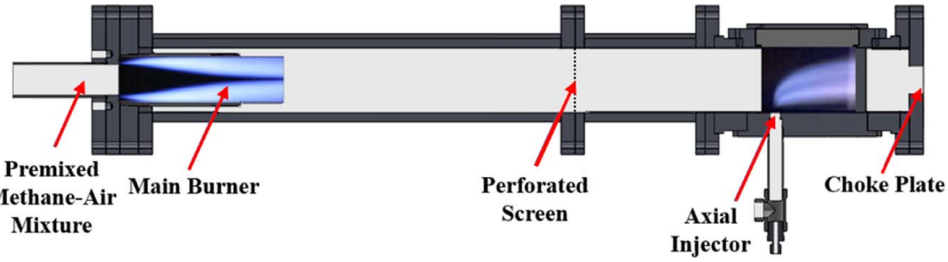

Fig. 2 Experimental axially staged combustor test facility

layer burning at low pressure and a receded jet core flame at elevated pressure level using a timescale analysis.

2 Experiment and Diagnostics

2.1 Combustor Configuration. The experimental facility is displayed in Fig. 2. The facility consists of a main stage burner where a burner pipe houses a lean premixed methane–air mixture. A perforated screen is located between the main and axial stage to aid flow uniformity. The test section contains three optically accessible windows for imaging diagnostics, and an interchangeable top plate used to introduce fully premixed mixture to the facility in the second stage. The axial injector has an exit diameter of 12.7 mm. At the downstream end of the facility, a choke plate with a diameter of 38.1 mm is used to choke the flow to the desired pressure level. Further details about the experimental setup and procedure could be found in Ref. [26].

At the exit of the choke pipe, a probe is placed in the center to capture exhaust gases for emissions measurements. The probe is large enough to capture a significant amount of gas to obtain a global average. Tests were done where the probe was traversed and the spatial location at the choke point did not have a significant effect on the measurements, confirming the obtained values accurately represent a global outlet average. The gases are carried through piping into a large ice bath to freeze any further reactions from occurring and condense out the water. A Horiba Mexa 584-L emissions analyzer was used to obtain nitrogen oxide levels. Unless mentioned otherwise, emission levels in this paper are dry and corrected to 15% oxygen. In the computational fluid dynamics (CFD), the main stage boundary was defined using the measured data. The dilution average was taken by evaluating mass-weighted surface average function one diameter after the jet penetrates. Outlet probe in the CFD was determined as a mass-weighted surface average at similar position six jet diameters downstream of the choke plate. Referenced probe positions are shown in Fig. 3.

2.2 Data Processing. Line-of-sight CH* chemiluminescence data at 200 μm per pixel spatial resolution were taken using a Photron Fastcam SA1.1 at a rate of 125 frames per second (fps) and a shutter speed of 1/1000; a narrowband 430 ± 2 nm filter was utilized to obtain CH* intensity. Since the CH* measured in the experiment corresponds to the chemiluminescent emission from CH species, the measured CH* concentration follows the CH concentration in the flame and a direct comparison with simulated CH species was deemed valid [27]. To replicate the experimental line-of-sight technique, simulated CH data were integrated along the z-axis. A $\Delta y/d = 0.05$ was selected for the integration, weighting all z-data equally. Accumulated sum of z and Δy data was normalized against the maximal area sum. Images were recorded with a resolution of 768×768 and were processed in MATLAB to obtain time-averaged images considering one second worth of data for each testing condition. The flame boundaries are determined based on Otsu's threshold method [28]. Particle image velocimetry (PIV) was performed using a dual-head 532 nm *Evergreen* laser with a time separation of 20 μs. The PIV data are processed in PIVLAB 2.00 using a contrast adaptive histogram equalization method (CLAHE). Figure 4 shows the overlay of planar turbulence intensity PIV data (blue plane) with simulated turbulence intensity (yellow-red 3D field), allowing an accurate representation of simulated data located at the z-symmetry plane.

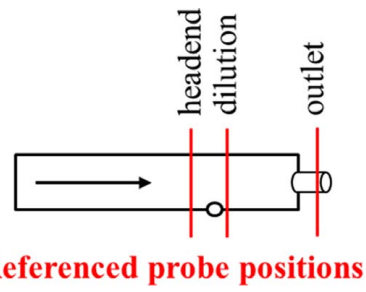

Fig. 3 Species probe positions referenced numerically and experimentally

3 STAR-CCM+ Computational Model

3.1 Configuration Domain. Figure 5 shows the hexahedral, locally refined STAR-CCM+ mesh grid used to describe the axial stage of the in-house test rig with a dump region attached downstream. The 29 million cell mesh grid consists of two separate mesh continua, connecting the axial stage (1) with dimensions $(x \times y \times z) = (195.1 \times 88.9 \times 38.1)$ mm to a choke pipe ($l = 73$ mm, $d = 38.1$ mm) and a dump region, and (2) linked with a conformal interface boundary. Grid convergence for the reacting jet trajectories, species reaction rates, and temperature profiles was ensured for the refinement level $\Delta s = 0.25$ mm. Position of local nitrogen oxide occurrence deviated for 19% with the 1 mm grid

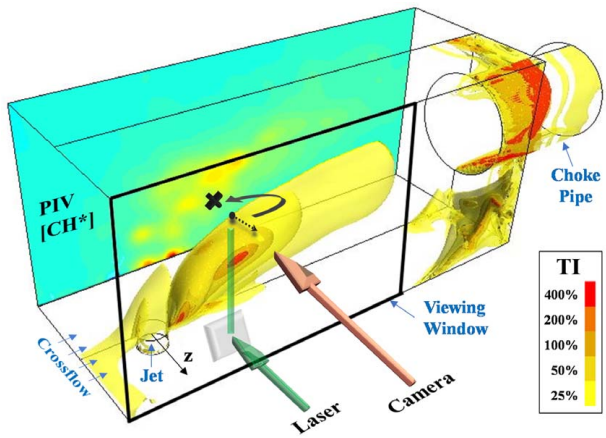

Fig. 4 CFD integrative data processing to match experimental PIV and line-of-sight CH* chemiluminescence data (Color version online.)

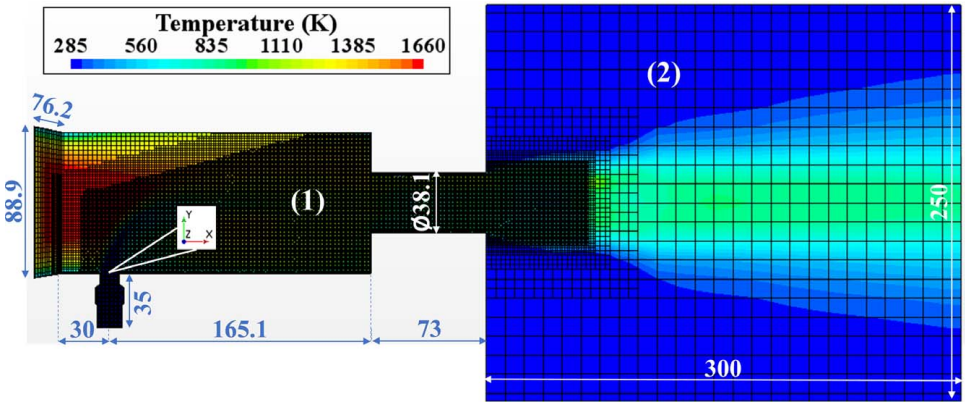

Fig. 5 Axial stage and dump region dimensions and CFD mesh grid

and for 4% with the 0.5 mm grid relative to the 0.25 mm grid. Nitrogen oxide reaction rates deviated for 46% at 1 mm and for 12% at 0.5 mm relative to the 0.25 mm grid. Hence, the latter resolution was used to refine the axial fuel line and combustion domain (1). A base size of 0.01 m was selected for the dump zone cells with a stepwise transition to the combustor outlet cell size ($\Delta s =$ 0.25 mm). Symmetricity along the z-axis was utilized. The global origin of the coordinate system was defined at the collision point between crossflow and jet centerline as shown in Fig. 5. Walls along the combustor and fuel line were defined at no-slip, smooth condition with the wall y^+ value set to 3 and wall heat transfer considered. Prism layer thickness was set to 0.4 mm. The domain of interest is the viewing window made of fused silica with thermal conductivity $k = 1.85$ W/(m K) at 700 K and $k = 1.4$ W/(m K) at ambient condition [29,30], covering 90% of the inner rig contact area before $x/d = 7$. Using its thickness $t = 25.4$ mm and a temperature difference $\Delta T = 500$ K across the window walls yields a boundary heat flux of -32.5 kW/m^2 (Eq. (4)):

$$\dot{q} = \frac{k}{s} \times \Delta T = \frac{1.65\ \text{W/(m K)}}{0.0254\ \text{m}} \times 500\ \text{K} = 32.5\ \text{kW/m}^2 \tag{4}$$

The estimate is reasonable, given that steady-state conditions are not reached due to rig run times being below 5 s paired with a strong main stage burner temperature profile. In addition, CFD and experimental data do not suggest any significant flame–wall interaction to occur along the windows [31]. Further downstream, 304 steel is the major wall component in use with a higher $k = 20$ W/(m K) at 700 K and $k = 16$ W/(m K) at 300 K [32,33]. The jet walls were defined at constant $T = 295$ K. The dump region (2) in Fig. 5 is specified as a separate external flow zone. The plane surrounding the interface boundary was defined as an inlet at stagnating velocity and ambient condition. Boundaries downstream of that plane are defined as outlets at ambient pressure.

3.2 Reactive Flow Description. Building upon previous numerical and experimental studies with a 4 mm axial jet [34–38], two STAR-CCM+ detailed chemistry models Laminar Flame Concept (LFC) and Eddy Dissipation Concept (EDC) were investigated for this study paired with the full GRI-Mech 3.0 [39]. The species transport equation is defined as follows (Eq. (5)):

$$\frac{\partial}{\partial t}\rho Y_i + \frac{\partial}{\partial x_j}(\rho u_j Y_i + F_{k,j}) = \omega_i \tag{5}$$

with Y_k being the species mass fraction, ω_i being the species reaction source term, and $F_{k,j}$ being the diffusion flux as a function of the turbulent Schmidt number. Both models consider the effect of turbulence on the combustion process implicitly through the increased turbulent diffusivity provided by the turbulence model. For premixed turbulent flames, the diffusivity can be enhanced by reducing the turbulent Schmidt and Prandtl numbers, resulting in a turbulent flame speed and thickness that are greater than if the cases were solely laminar. Detailed chemistry is solved for a Constant Pressure Reactor with a stiff ODE solver to integrate the chemical source terms, allowing a reaction system with a wide range of reaction time scales. The integration of chemical state is defined in Eq. (6) with τ being the time-step and r_k denoting the species reaction rate [23,40]:

$$Y_i^* = Y_i + \int_0^\tau r_k(\mathbf{Y}, T, p)dt \tag{6}$$

The right side of the species transport equation (5) defines the source term as a function of density ρ, mean reaction rate multiplier f, mass fraction, and time-step, shown in Eq. (7):

$$\omega_i = \rho f\left(\frac{Y_i^* - Y_i}{\tau}\right) \tag{7}$$

For steady simulation with the LFC, the time scale is expressed by the residence time in the cell. The LFC (Fig. 6, red line B) models the reacting jet-in-crossflow situation as an accelerated laminar flame with weak turbulence–chemistry interaction [23], hence f in Eq. (7) is set to 1. Instantaneous reaction rate is evaluated for the mean temperature, pressure, and species fraction. An early ignition at $x/d = 2.5$ was determined with the LFC. Reaction rates in the flame front were overpredicted by two to three orders of magnitude, resulting in a crescent flame shape and local CH concentration being consumed to all sides, even in the direction facing the main stage burner. The *Laminar Flame Concept* could be valid for premixed, partially premixed, and unsteady flames [23]; however, it was not rated suitable for this turbulence-dominated, strongly finite-rate jet-in-crossflow flame configuration. Similarly, any Flamelet approach with tabulated GRI-Mech 3.0 parameters would mispredict the flame position with an early lee-side ignition event, shown by the blue crosses (A) in Fig. 6. The finite-rate EDC considers turbulence–chemistry interaction additionally in Eq. (7) with a rate multiplier $f < 1$. The rate multiplier is defined in Eq. (8):

$$f = \left(\left[C_l\left(\frac{\nu\tau_{turb}}{L^2}\right)^{0.25}\right]^{-3} - 1\right)^{-1} \tag{8}$$

with C_l being the fine structure length constant, υ being the kinematic viscosity, τ_{turb} being the turbulent time scale, and L being the turbulent length scale. Using the EDC, time-step from Eq. (7) is defined as follows (Eq. (9)):

$$\tau = F_{\text{CFL}}\tau_{turb} \tag{9}$$

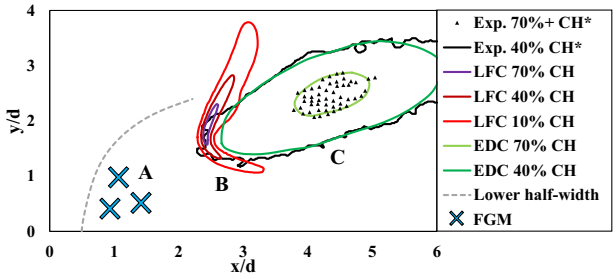

Fig. 6 CFD jet-in-crossflow modeling at $p = 5$ atm: A, FGM; B, Laminar Flame Concept; C, Eddy Dissipation Concept (Color version online.)

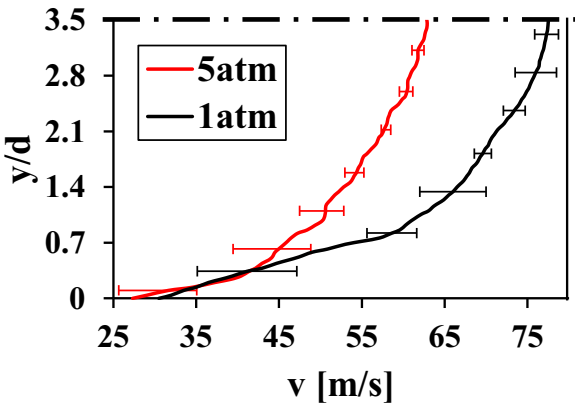

Fig. 7 Averaged main stage PIV velocity profiles at pressure levels 5 atm and 1 atm

with F_{CFL} being the CFL scaling factor. The EDC time-step is close to the smallest turbulent eddy (Kolmogorov) time scale; hence, the effect of turbulence is modeled as a reduction of the mean reaction rate relative to the LFC [23]. The EDC did a significantly better job describing the reactive zone, showing CH concentration (Fig. 6, green lines (C)) in good agreement with the experimental data (black line). A slightly thicker CH flame front is followed by a broader domain of CH consumption, which is located solely downstream of the flame. Figure 6 shows the resulting overlay of CH concentration with the Eddy Dissipation Concept and the experimental verification with the CH* chemiluminescence data. Maximum CH levels are found between $x/d = 4$ and $x/d = 5$. The EDC fine structure factors were used at their default value. Turbulent Schmidt and Prandtl numbers were lowered from a default 0.7–0.5, which is in the range proposed by Tominagaa and Stathopoulos [41] to pronounce Reynolds-averaged Navier–Stokes (RANS) turbulent momentum diffusion, follows the recommendation of Refs. [23,40] for highly strained flows and was used for a similar axially staged configuration by Loparo [42]. The correction helped move the flame slightly back upstream and pronounce the spread of the radical domain as observed from the experimental CH* data. A slight underprediction of modeled horizontal CH spread has remained. The CFD simulation uses finite-rate chemistry to close the reaction rate, leveraging the full GRI-Mech 3.0 to provide species reaction rates and thermodynamic properties for the integration of finite kinetics. The use of a finite-rate chemistry model is in agreement with numerical investigations of Prathap et al. [22] that used an axial-staged combustor at similar operating conditions. EDC simulated Damköhler numbers in the flame ranged up to 0.31 at pressure, and this value was confirmed with calculated results, amounting up to 0.44 with a laminar flame speed of 7.1 cm/s (determined with a 1D premixed laminar flame combustor and compared with literature data [43] for lean CH_4 combustion at $p = 5$ atm) and turbulent fluctuations of 10 m/s as determined from the PIV data (Fig. 7).

The hot gas composition entering from the main burner was determined with an equilibrium calculation, using a constant pressure/enthalpy reactor. Equilibrium mass fractions of nine species CO, CO_2, H_2, H_2O, HO_2, N_2, O, O_2, and OH were complemented with measured NO and NO_2 main stage burner levels. Results for the main stage species boundary condition at $p = 5$ atm are summarized in Table 1. A weak pressure dependency was found for the equilibrium at lower pressure, and main species remained near constant.

3.3 Turbulent Flow Field. A coupled flow model with multicomponent diffusion was required to account for the compressible flow field and the domain of choked flow. Material properties were determined with mass-weighted mixture and Sutherland's law method [40]. The k–ω γ-Re_θ shear stress transport (SST) model was used and in relatively good agreement with the data. At the main stage outlet, a developing flow profile was determined for all pressure levels investigated. PIV velocity profiles are shown in Fig. 7. At 1 atm, the mass flows needed to be increased relative to the scaling law due to stability limits of the experimental high-pressure facility. Despite the increase of mass flow, the momentum flux ratio remained constant among the cases. Profiles at 3 atm and 5 atm were near-identical due to the linearly scaled condition.

Maximum uncertainty was calculated to be 13% from the PIV data located in the near-wall domain. The measured main stage PIV profiles are reasonable, given the short entry length of $x/d_h = 10$ from the main stage inlets. Profiles in Fig. 7 defined the CFD crossflow boundary condition, and the γ-Re_θ transition function was defined to allow up to 25 mm thickness of hydrodynamic boundary layer. An accurate description of the reacting jet trajectory

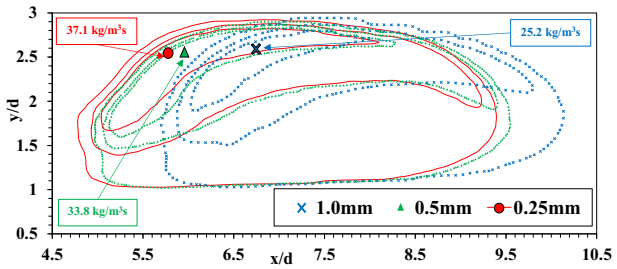

Fig. 8 Production rate iso-levels 1 kg/(m^3 s), 10 kg/(m^3 s), and 20 kg/(m^3 s) of CO_2 for three grid levels $\Delta s = 0.25$ mm (red), 0.5 mm (green), and 1.0 mm (blue) (Color version online.)

Table 1 Main stage burner species equilibrium calculation and measured NO_x data

φ_{main}	p (atm)	T_0 (K)	T_{equ} (K)	ρ_{equ} (kg/m^3)	Y_{CO}	Y_{CO_2}	Y_{H_2}
0.58	5	295	1733	0.98	9.0×10^{-6}	8.9×10^{-2}	/
Y_{H_2O}	Y_{HO_2}	Y_{N_2}	Y_{NO}	Y_{NO_2}	Y_O	Y_{OH}	Y_{O_2}
8.7×10^{-2}	1.0×10^{-6}	7.4×10^{-1}	1.4×10^{-5}	2.0×10^{-6}	4.0×10^{-6}	1.6×10^{-4}	8.2×10^{-2}

Table 2 Test matrix with a 12.7 mm lean premixed axial jet at three pressure levels

Main burner stage					Axial stage				
			Centerline						
$\dot{m}_{main}^{CH_4}$ (g/s)	$\dot{m}_{main}^{air}$ (g/s)	φ_{main} (−)	T_{main} (K)	v_{main} (m/s)	$\dot{m}_{Jet}^{CH_4}$ (g/s)	$\dot{m}_{Jet}^{air}$ (g/s)	φ_{Jet} (−)	T_{Jet} (K)	p (atm)
14.46	430.6	0.58	1610	62	2.52	48.7	0.75	290	5
8.65	213.1			64	1.51	29.2			3
4.57	112.5			80	0.80	15.4			1

was achieved and proven in previous work [36]. The crossflow TI profile was determined from the PIV to rise from 15% at the centerline to about 30% along the wall. Turbulence intensity at the jet was set to 6%, and turbulent length scales were set to $L = 5$ mm at the main stage boundary and $L = 1$ mm at the jet, respectively.

3.4 Grid Convergence Study. A grid convergence study was done by variation of the grid refinement in the critical jet and reactive domain between levels $\Delta s = 0.25$ mm (29 million cells), $\Delta s = 0.5$ mm (4.5 million cells), and $\Delta s = 1.0$ mm (0.7 million cells). Target was to show the influence of coarser mesh size and to determine possible tradeoffs that could be acceptable to mesh larger combustors for industry use. Figure 8 shows the CO_2 production rate plotted at iso-levels 1 kg/(m^3 s), 10 kg/(m^3 s), and 20 kg/(m^3 s).

Whereas a sharp iso-levels contour at the upstream-most position was determined for the $\Delta s = 0.25$ mm grid (Fig. 8, red lines), some amount of numerical dissipation was recorded with the 0.5 mm grid (Fig. 8, blue crosses) and significant deviations were shown for the 1 mm grid (Fig. 8, green dots) in terms of the flame position and production levels. Details about the flame-counter rotating vortex pair (CVP) interaction are depicted less accurately upon transition to the coarser grids. Horizontal flame liftoff is strongly dependent on the mesh grid used and was shown to be 4% overpredicted for the 0.5 mm grid and 19% overpredicted with the 1 mm grid (relative to the 0.25 mm grid). Vertical flame liftoff Δy was relatively unaffected. Maximum CO_2 production rate is strongly grid dependent, transition from $\Delta s = 0.25$ mm to 0.5 mm reduced the maximum rate by 9%, and transition from 0.25 mm to 1 mm reduced the rate by 32%. End positions of significant CO_2 production were found to be 8% delayed for the 1 mm grid and 2% delayed for the 0.5 mm grid relative to the 0.25 mm grid. A CentOS 7 cluster was used with Intel Xeon cores, x86_64 architecture with 28–32 cores per node and 128–192 GB RAM. A Lustre parallel file system with 56 Gbit/s 4x FDR InfiniBand network fabric was used to transfer data. Power demand for a detailed chemistry simulation with 29 million cells was 20,000 CPU hours at dampened under-relaxation factor settings.

3.5 Test Matrix. Mass flows were linearly scaled to operate at various pressure levels, keeping the fuel split, equivalence ratios, and flow profiles near constant. The influence of pressure reduction from 5 atm to 3 atm and 1 atm was investigated with a lean $\varphi_{main} = 0.58$ and a lean premixed $\varphi_{Jet} = 0.75$ axial jet. The boundary conditions used to simulate the investigated operating points are stated in Table 2.

4 Results and Discussion

4.1 Nitrogen Oxide Emission. A comparison of the simulated and experimental NO levels determined at the choke pipe outlet position (as described in Sec. 2.1) is summarized in Table 3.

Trend for the main burner nitric oxide (NO) levels is in agreement with Refs. [5,44] and was determined to scale with $p^{0.4}$. Global NO outlet emission was found to scale with $p^{-0.55}$ for both the CFD and experimental data (Eq. (10)). A global definition in the equation form was stated by using the NO emission level

Table 3 Corrected nitrogen oxide emission with a lean premixed 12.7 mm axial jet

φ_{main} (−)	φ_{Jet} (−)	p (atm)	$NO_{main,Exp.}$ (ppm)	$NO_{outlet,Exp.}$ (ppm)	$NO_{outlet,CFD}$ (ppm)
0.58	0.75	5	5.0	5.5	5.9
		3	4.0	8.0	8.8
		1	2.5	14.0	15.5

at 1 atm as a reference point (Fig. 9). Elevated pressures allow an axial NO_x benefit due to the reduced axial flame surface and higher amount of axial burning in the jet core (compare with Sec. 4.2)

$$X_{NO,global} = f(p^{-0.55}) \tag{10}$$

Experimental pressure measurement was relatively accurate with a deviation of ±25 kPa at pressure and ±35 kPa at atmospheric condition. Accuracy of the experimental NO measurement was limited by the accuracy of the gas analyzer; increased positive emission uncertainty was stated for the experimental 1 atm condition since the combustion event may have been just near complete in the given facility length. Measured outlet unburned hydrocarbons (UHC) levels remained low (3 ppm).

4.2 Local Flame and Nitrogen Oxide Occurrence. The influence of pressure reduction from 5 atm to 1 atm on the reaction timescale and local NO levels was investigated in Figs. 10(*A*) and 10(*B*). To characterize the flame, CFD data for the molar concentration of CH were processed by evaluating line integrals along the z-direction at $x/d = 5$ (Fig. 10(*C*)). Uncertainty of CH* signal (Figs. 10(*C*) and 11(*C*)) ranged up to $I/I_{max} = \pm 0.1$ due to turbulent fluctuations of the flame and flow field. To obtain the correct result for the x/d plane (Fig. 10(*C*)), a $\Delta y = 0.05$ was selected and all z-values in the increment added up and normalized with respect to the sum at the maximum concentration level (compare with

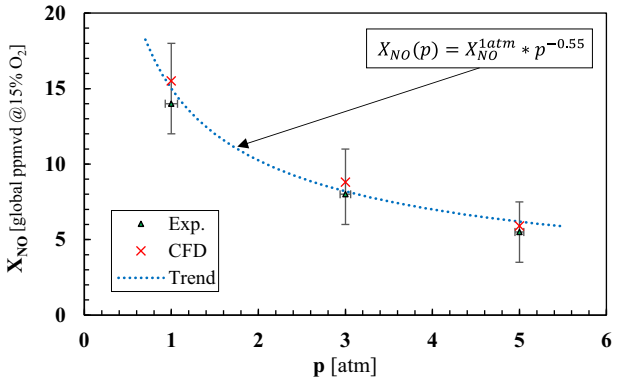

Fig. 9 Pressure dependency of global NO emission at $T_{outlet} = 1700$ K

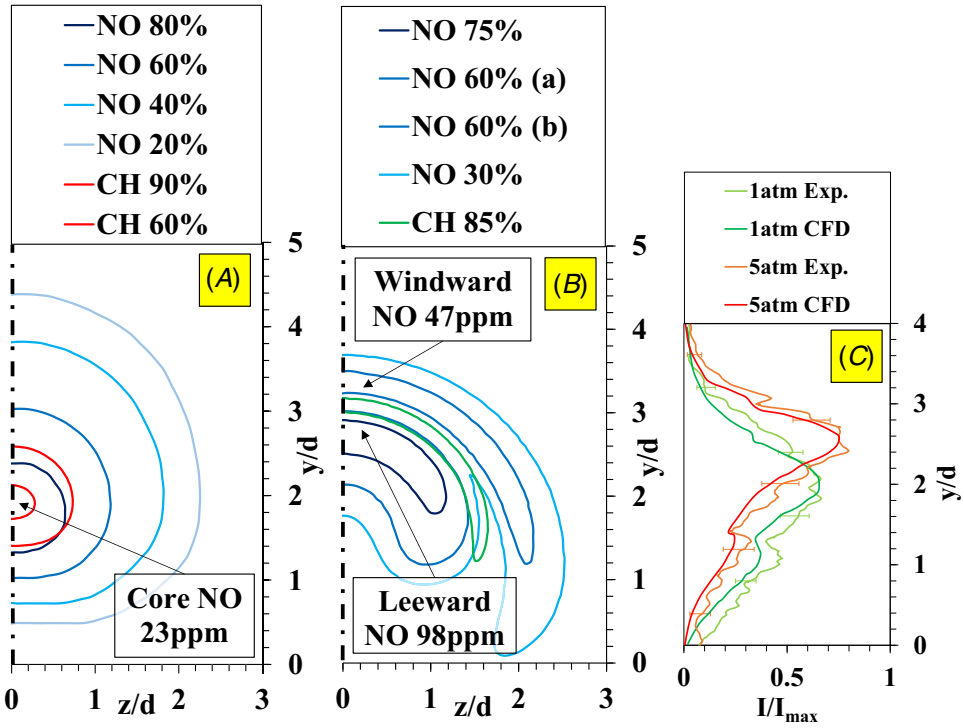

Fig. 10 $\varphi_{main} = 0.58$, $\varphi_{Jet} = 0.75$, position $x/d = 5$: CH and NO concentration (CFD) along the y,z directions: (*A*) $p = 5$ atm, (*B*) $p = 1$ atm, and (*C*) CH* (experimental) and CH (z-integrated CFD) along the y-direction (Color version online.)

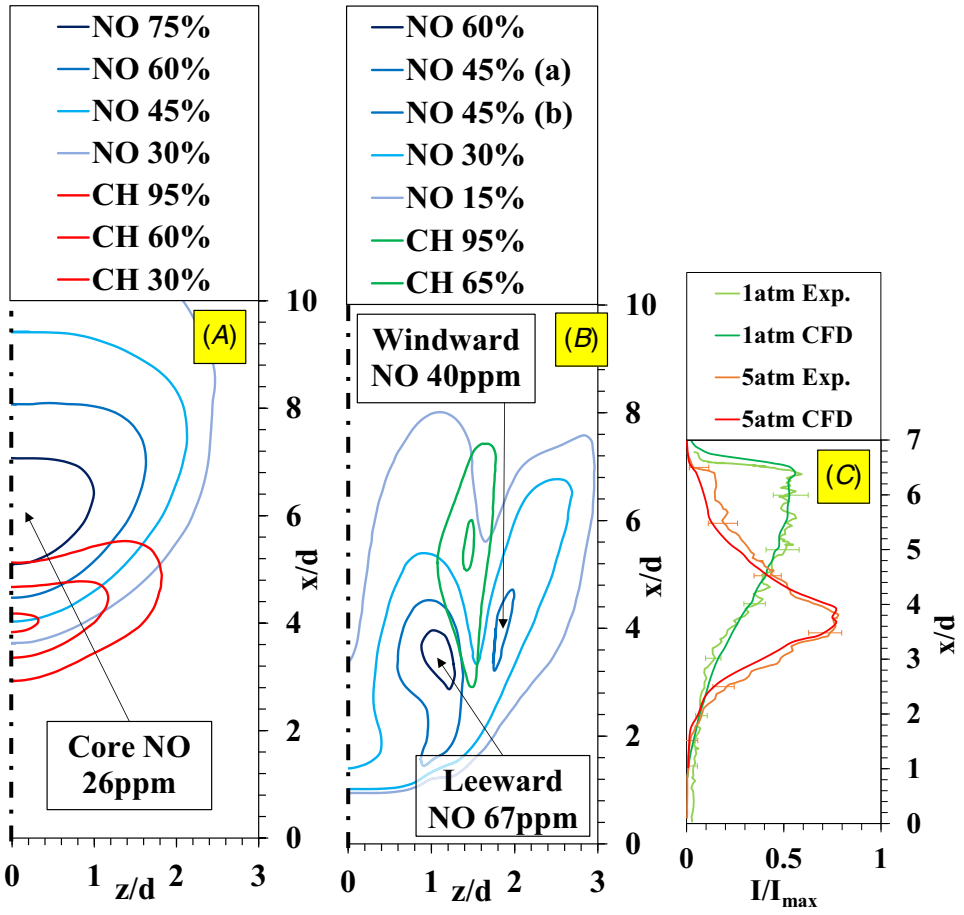

Fig. 11 $\varphi_{main} = 0.58$, $\varphi_{Jet} = 0.75$: CH and NO concentration (CFD) along the x,z directions: (*A*) $p = 5$ atm, (*B*) $p = 1$ atm, and (*C*) CH* (experimental) and CH (z-integrated CFD) along the x-direction (Color version online.)

Sec. 2.2). Figures 10(*A*) and 10(*B*) ($p = 5$ atm, $p = 1$ atm) plot normalized CH and NO mole fraction data along y and z at a position $x/d = 5$ downstream of the jet. The 5 atm core flame shows NO production levels (blue lines) in spatial agreement with the CH levels (red line). Maximum NO level in the core is 23 ppm, and pronounced spread is found at the windward side due to proximity of the hot crossflow. At 1 atm, the near-flame domain (green line) separates two branches of NO occurrence (blue lines). Maximum NO level of 98 ppm can be found at the leeward side, indicating that convective transport at the CVP center is not enough to entirely inhibit NO levels accumulating in the domain between the flame front and the vortex center. Figure 10(*C*) shows the verification of z-integrated CH from the CFD with experimental CH* chemiluminescence data at the position $x/d = 5$, plotting the y/d axis against the normalized intensity level. Both CFD flames show CH levels in a domain between $y/d = 0$ and $y/d = 4$ and follow the measured data with deviations below 20%. Maximum z-accumulated CH intensity can be found at $y/d = 2$ for the shear layer flame ($p = 1$ atm), denoted by the green line in Fig. 10(*C*). At $p = 5$ atm, the red line (Fig. 10(*C*)) represents a higher maximum CH level for the core flame, found at $y/d = 2.5$. At $x/d = 5$ (Fig. 10(*A*)), the $p = 5$ atm data show a core flame burning close to the symmetry plane, exhibiting minor changes in the CH profile by the contribution of the z-data. The line integration method described above was particularly critical to match the $p = 1$ atm flame (Fig. 10(*B*)), considering shear layer burning with a contribution of simulated CH signals up to two jet diameters off the symmetry plane.

A similar analysis from a top view (at constant position $y/d = 2$) is depicted in Fig. 11. Compared were simulated CH and experimental CH* chemiluminescence data at $p = 5$ atm (Fig. 11(*A*)) and $p = 1$ atm (Fig. 11(*B*)) as well as the z-integrated CH signal for verification (Fig. 11(*C*)). At $p = 5$ atm, the CH tailing phenomenon shown in Fig. 11(*C*) can be tracked in the x,z-space: Fig. 11(*A*) shows decaying NO levels toward the outlet. This behavior suggests produced NO to be either transported to higher y/d positions by the CVP or to be further oxidized to NO_2 in the low temperature domain facing the bottom wall. The $p = 1$ atm data (Fig. 11(*B*)) validate statements made for Fig. 10. The top view of the two NO branches is shown to be separated by the shear layer flame front. NO levels trapped at the inside of the CVP reach peak levels of 67 ppm. A less steep slope with lower maximum intensity at $x/d = 6$ proves the slower reaction progress in the shear layer. CH levels were fully consumed before $x/d = 7$ (Fig. 11(*C*), light green), and this behavior was verified with the CFD (Fig. 11(*C*), dark green).

A comparison of the 5 atm and 1 atm total peak areas in Figs. 10 and 11 indicates that similar total CH amounts are present throughout the plane, and the z-data revealed that local distribution plays a significant role for the emissions results. Based on the data analyzed, pressure is seen to aid with lowering the production of NO_x emissions in the axial stage as a result of the occurring flame stabilization mechanism. Experimental data underline the significant influence of pressure on emission levels. At $p = 5$ atm, 5.0 ppm NO at 15% oxygen was measured after the main stage and 5.5 ppm at the axial stage outlet. In contrast, at atmospheric pressure, 2.5 ppm was determined after the main stage and 14 ppm at the axial outlet. The concept of axial staging is relatively ineffective at low pressure but significant emission saving potential was proven at lab-scale high-pressure level 5 atm.

4.3 Turbulence Intensity. To get a certain amount of insight to the turbulent scales, simulated and experimental turbulence intensities at the lee-side recirculation zone ($x/d = 2.5$) are compared in Fig. 12. Experimental PIV data were time-averaged and filtered to obtain relatively smooth turbulence intensity profiles with maximum errors of 20% (Fig. 12(*a*)). A significant pressure dependency of local turbulence intensities at the jet lee-side was

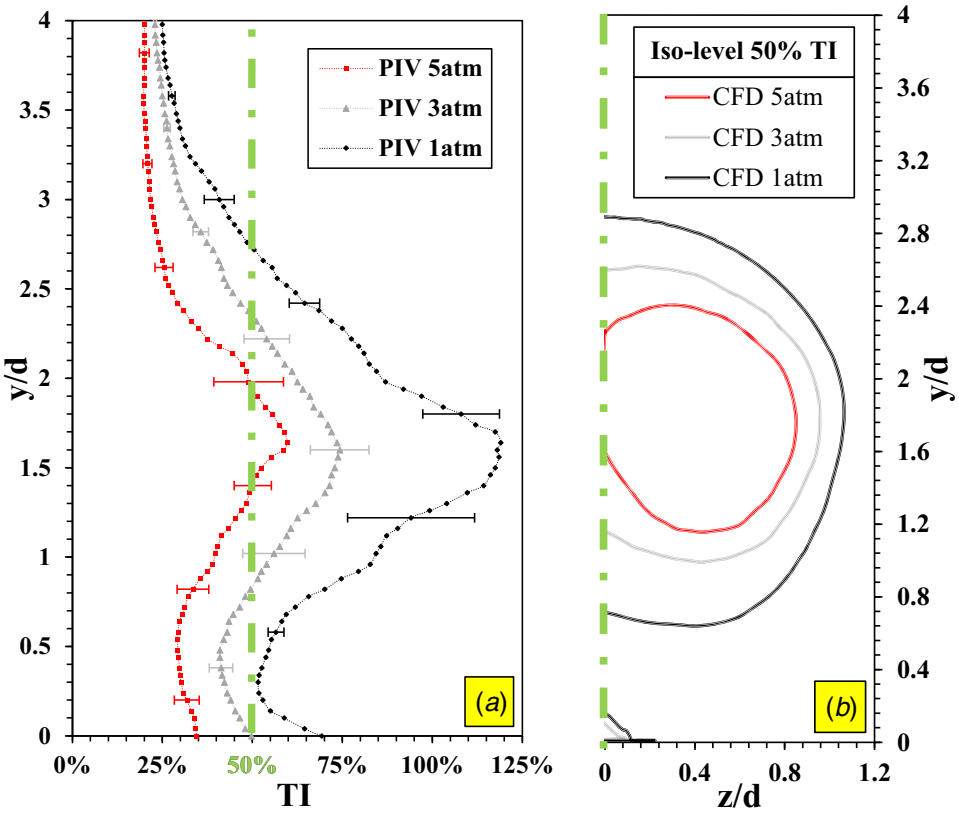

Fig. 12 Turbulence intensities in the recirculation zone at three pressure levels: (*a*) filtered PIV data and (*b*) perpendicular *y*,*z* plane with 50% TI iso-level from the CFD (Color version online.)

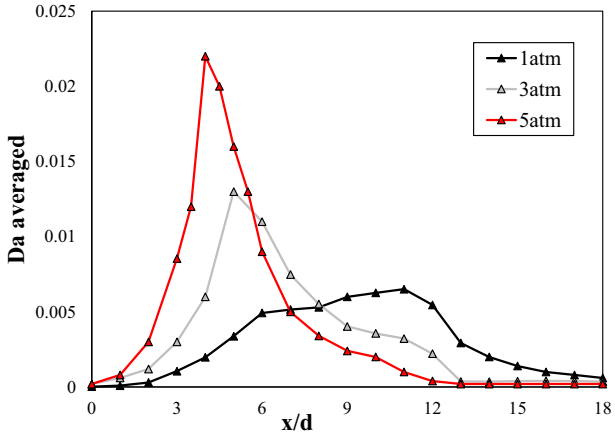

Fig. 13 Averaged Damköhler number at three pressure levels along the axial stage

determined. Maximum intensity levels at a position $y/d = 1.7$ were found to be 60% at 5 atm, 75% at 3 atm, and 115% at atmospheric condition. Beyond the windward trajectory edge, turbulence intensity shows a weak pressure dependency within levels of 20% and 25% (Fig. 12(*a*)), and these levels were found in the CFD as well. Figure 12(*b*) shows the simulated y,z field of turbulence intensity 50% iso-levels at the similar position $x/d = 2.5$. The CFD trend shows a more pronounced recirculation zone at lower pressure level. Since the PIV technique is well focused on the centerline by using a collimated laser sheet, the centerline axis ($z = 0$) of simulated 50% iso-level can be used for comparison with the profile found at a TI level of 50% in the PIV data. The evaluated position for this perpendicular comparison is highlighted with the green dashed lines in Figs. 12(*a*) and 12(*b*). The line profiles are relatively similar and suggest the RANS k–ω γ-Re_θ SST model with intensity and dissipation boundary conditions defined in Sec. 3.3 to give a good approximate description of the turbulent scales and their variation with system pressure.

4.4 Timescale Comparison. The analysis of the present time scales at different pressure levels is described in this section. Averaged trends of the Damköhler number throughout the combustor are investigated in Fig. 13.

Mass-weighted y,z surface average of the Damköhler number was evaluated with an increment of $x/d = 1$. For the $p = 5$ atm condition, average was evaluated with an increment $x/d = 0.5$ to capture the steep rise of Da at the flame. At $p = 5$ atm, a distinct maximum was recorded with a certain amount of tailing toward the combustor outlet. At $p = 3$ atm, the similar trend was found but dampened due to the lower operating pressure. In contrast, a significant deviation is shown at atmospheric pressure. Combustion event is delayed, and maximum Damköhler number is reached after $x/d = 10$.

Due to the occurrence of local combustion event along the jet shear layer (particularly at low pressure), further analysis is required to quantitatively compare Damköhler numbers. Figure 14 shows the y- and z-directions at two distinct positions $x/d = 5$ and 10 downstream of the axial jet. At $p = 5$ atm, elevated local Damköhler number $\mathrm{Da} = 0.31$ was found after $x/d = 5$ at the flame, located at the windward trajectory edge. A certain amount of jet core burning was recorded as shown by the relatively wide reactive domain. Combustion is near complete at $x/d = 10$, and production of post-flame NO remains as a weak signal. At $p = 3$ atm, maximum local Damköhler number $\mathrm{Da} = 0.095$ is found at the windward edge. Reactions take place in a thinner domain at $p =$ 3 atm (Fig. 14) that surrounds the jet more. Similarly, reaction is relatively complete at $x/d = 10$. Pressure reduction to $p = 1$ atm shows a significantly lower $\mathrm{Da} = 0.012$ and distinct change in the reaction kinetics. Shear layer burning is concentrated in the CVP, and the flame may interact locally with the vortex center. At $p =$ 1 atm, reaction progress is slow and significant reaction activity is

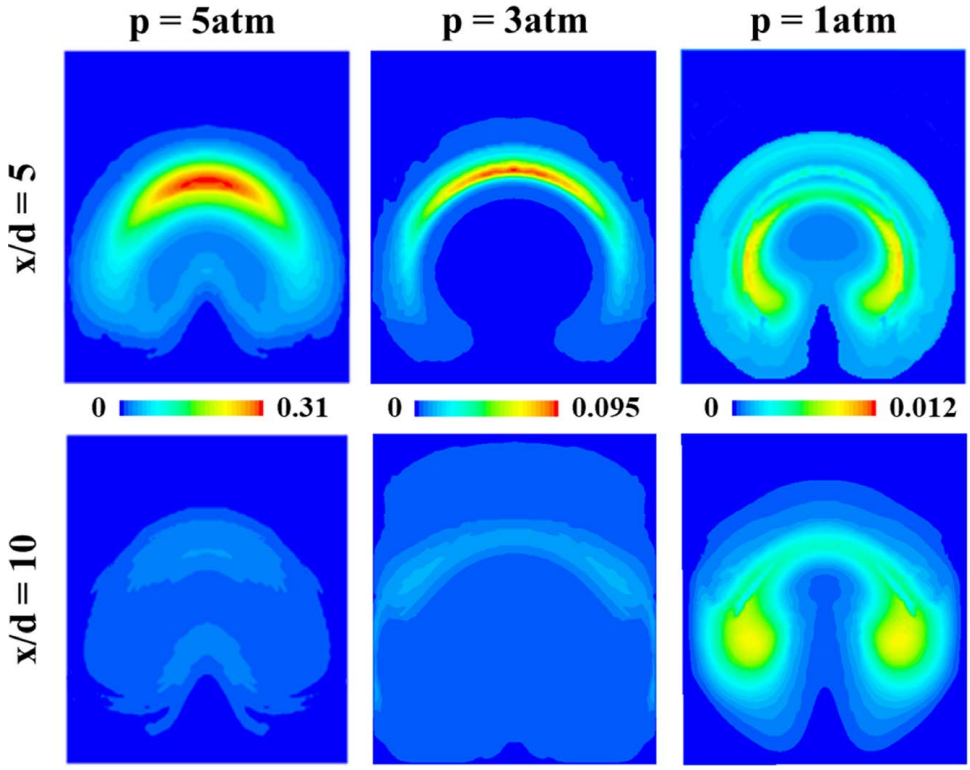

Fig. 14 Local Damköhler number at three pressure levels and two positions downstream of the axial jet

present at $x/d = 10$. Applying the gained knowledge with the analysis in Secs. 4.1 and 4.2, the reason for high NO formation at low pressure is shown in Fig. 14. Due to the reduced bimolecular collision rate as a function of $\mathrm{Da} \sim p^2$, a longer (x/d direction) flame with more radial surface area (y/d, z/d) produces more radicals and favors elevated NO production. In contrast, at $p = 5$ atm, a relatively short, receded jet core flame is located at the windward trajectory side, allowing a significantly smaller flame surface and reduced NO levels, despite the locally higher temperature level.

5 Conclusion

This paper investigates lean premixed 12.7 mm axial jets in vitiated crossflow with detailed chemistry and 53 species considered. All operating points were validated against in-house experimental data and found to be in the finite-rate regime. Simulated exit nitrogen oxide levels were validated with experimental emission data, and a global emission trend for the pressure dependency of corrected nitrogen oxide emission was found to be $X_{\mathrm{NO},global} = f(p^{-0.55})$ for the investigated turbine inlet temperature level $T = 1700$ K. A substantial difference about the reaction kinetics and local nitrogen oxide production was pointed out for the pressure dependent transition between two flame types. At elevated pressure of 5 atm, jet core burning was determined at relatively high Damköhler number of 0.3. A receded core flame with a compact flame surface produced a moderate amount of NO emission along the jet core. High windward thermal NO emission was avoided due to the moderate temperature level used in this study. At atmospheric pressure, prolonged shear layer burning at low $\mathrm{Da} = 0.015$ was determined to cause the elevated amount of nitrogen oxide emission. The physical reason was tracked with an analysis of the reaction time scale. The flame surrounded the entire shear layer and combustion required twice the axial length relative to combustion at pressure. Result was a large flame surface and high accumulation of NO at both sides of the shear layer. A $\mathrm{Da} \sim p^2$ dependency of the local Damköhler number was determined for the transition between shear layer burning and jet core burning. Chemical timescales were shown to match with experimental data by an analysis of the CH* chemiluminescence signal and simulated CH concentration in the flame. In contrast, a moderate pressure dependency was determined for the contribution of the turbulent timescales. Higher turbulence intensity along the lee-side recirculation zone of the jet at lower pressure was shown with an overlay of the PIV data and simulated turbulence intensities.

Acknowledgment

The authors (BS, TG, MO, KA, and SM) acknowledge support from the Department of Energy under Award Number DE-FE0031227 and collaboration with Dr. Carlos Velez and GE Global Research. This report was prepared as an account of work sponsored by an agency of the United States Government. Neither the United States Government nor any agency thereof, nor any of their employees, makes any warranty, express or implied, or assumes any legal liability or responsibility for the accuracy, completeness, or usefulness of any information, apparatus, product, or process disclosed, or represents that its use would not infringe privately owned rights. Reference herein to any specific commercial product, process, or service by trade name, trademark, manufacturer, or otherwise does not necessarily constitute or imply its endorsement, recommendation, or favoring by the United States Government or any agency thereof. The views and opinions of authors expressed herein do not necessarily state or reflect those of the United States Government or any agency thereof.

Conflict of Interest

There are no conflicts of interest.

Data Availability Statement

The datasets generated and supporting the findings of this article are obtainable from the corresponding author upon reasonable request. The authors attest that all data for this study are included in the paper. Data provided by a third party are listed in Acknowledgment. No data, models, or codes were generated or used for this paper.

Nomenclature

d = jet diameter (m)
k = thermal conductivity (W/(m K))
l = length (m)
p = pressure (atm)
s = cell dimension (m)
t = thickness (m)
u = velocity (m/s)
x = axial coordinate, downstream position (m)
y = perpendicular coordinate, penetration depth (m)
z = lateral coordinate (m)
$\dot{m}$ = mass flowrate (kg/s)
$\dot{q}$ = heat flux (W/m^2)
$\dot{w}$ = reaction rate (g/(m^3 s))
J = momentum flux ratio
L = turbulent length scale (m)
T = temperature (K; °C)
X = mole fraction
Y = mass fraction
y^+ = wall criterion
Da = Damköhler number
ppmvd = parts per million on volumetric, dry basis
RST = Reynolds Stress Turbulence

Greek Symbols

γ-Re$_\theta$ = transition model
Δ = difference
ε = turbulent dissipation rate
ρ = density
τ = time scale
φ = equivalence ratio
ω = vorticity

Subscripts and Superscripts

axial = axial stage
chem = chemical
exp = experimentally measured
global = entire combustor
jet = axial jet
main = main burner stage
max = maximum
turb = turbulent

References

[1] Laster, W. R., Martin, S. M., Bilbao, J. E. P., Hardes, J., and Fox, T. A., 2018, "Dual Outlet Nozzle for a Secondary Fuel Stage of a Combustor of a Gas Turbine Engine," Patent US 10,139,111 B2, Siemens Energy, Inc.
[2] Martin, S. M., Cai, W., and Harris, J., 2013, "Apparatus and Method for Controlling the Secondary Injection of Fuel," Patent US 8,387,398 B2, Siemens Energy, Inc.
[3] Venkataraman, K. K., Washam, R. M., Karim, H., Terry, J. C., and Davis, L. B., 2014, "Late Lean Injection System Configuration," Patent US 8,701,383 B2, General Electric Company.
[4] Venkataraman, K. K., Terry, J. C., Velkur, C. B., and Karim, H., 2014, "Late Lean Injection Fuel Staging Configurations," Patent US 8,707,707 B2, General Electric Company.
[5] Elkady, A. M., Herbon, J., Kalitan, D. M., Leonard, G., Akula, R., Karim, H., and Hadley, M., 2012, "Gas Turbine Emission Characteristics in Perfectly Premixed Combustion," ASME J. Eng. Gas Turbines Power, **134**(6), p. 061501.

[6] Gollahalli, S. R., and Pardiwalla, D., 2002, "Comparison of the Flame Characteristics of Turbulent Circular and Elliptic Jets in a Crossflow," ASME J. Energy Resour. Technol., **124**(3), pp. 197–203.
[7] Al-Malak, A., Elshafei, M., Habib, M. A., and Al-Zaharnah, I., 2016, "Soft Analyzer for Monitoring NO_x Emissions From a Gas Turbine Combustor," ASME J. Energy Resour. Technol., **138**(3), p. 031101.
[8] Kibrya, M. G., and Karim, G. A., 1996, "Blowout Limits of a Jet Diffusion Flame in the Presence of Small Surrounding Jet Pilot Flames," ASME J. Energy Resour. Technol., **118**(2), pp. 140–144.
[9] Moore, N. J., Terry, S. D., and Lyons, K. M., 2011, "Flame Hysteresis Effects in Methane Jet Flames in Air-Coflow," ASME J. Energy Resour. Technol., **133**(2), p. 022202.
[10] Askari, O., Metghalchi, H., Hannani, S. K., Hemmati, H., and Ebrahimi, R., 2014, "Lean Partially Premixed Combustion Investigation of Methane Direct-Injection Under Different Characteristic Parameters," ASME J. Energy Resour. Technol., **136**(2), p. 022202.
[11] Liu, S., Yin, H., Xiong, Y., and Xiao, X., 2017, "A Comparative Analysis of Single Nozzle and Multiple Nozzles Arrangements for Syngas Combustion in Heavy Duty Gas Turbine," ASME J. Energy Resour. Technol., **139**(2), p. 022004.
[12] Elgammal, T., and Amano, R. S., 2018, "Effectiveness of Central Swirlers in the Thermal Uniformity of Jet-in-Crossflow Mixing," ASME J. Energy Resour. Technol., **140**(10), p. 101202.
[13] Khalil, A. E. E., Gupta, A. K., Bryden, K. M., and Lee, S. C., 2012, "Mixture Preparation Effects on Distributed Combustion for Gas Turbine Applications," ASME J. Energy Resour. Technol., **134**(3), p. 032201.
[14] Khalil, A. E. E., and Gupta, A. K., 2014, "Dual Injection Distributed Combustion for Gas Turbine Application," ASME J. Energy Resour. Technol., **136**(1), p. 011601.
[15] Safari, M., and Sheikhi, M. R. H., 2014, "Large Eddy Simulation for Prediction of Entropy Generation in a Nonpremixed Turbulent Jet Flame," ASME J. Energy Resour. Technol., **136**(2), p. 022002.
[16] Deng, X., Xiong, Y., Yin, H., and Gao, Q., 2016, "Numerical Study of the Effect of Nozzle Configurations on Characteristics of MILD Combustion for Gas Turbine Application," ASME J. Energy Resour. Technol., **138**(4), p. 042212.
[17] Emami, M. D., Shahbazian, H., and Sunden, B., 2019, "Effect of Operational Parameters on Combustion and Emissions in an Industrial Gas Turbine Combustor," ASME J. Energy Resour. Technol., **141**(1), p. 012202.
[18] Saini, P., Chterev, I., Pareja, J., Aigner, M., and Boxx, I., 2020, "Effect of Pressure on Hydrogen Enriched Natural Gas Jet Flames in Crossflow," Flow Turbul. Combust., **105**, pp. 787–806.
[19] Fleck, J. M., Griebel, P., Steinberg, A. M., Arndt, C. M., and Aigner, M., 2013, "Auto-Ignition and Flame Stabilization of Hydrogen/Natural Gas/Nitrogen Jets in a Vitiated Cross-Flow at Elevated Pressure," Int. J. Hydrogen Energy, **38**(36), pp. 16441–16452.
[20] Fleck, J. M., Griebel, P., Steinberg, A. M., Stöhr, M., and Aigner, M., 2010, "Experimental Imvestigation of a Generic, Fuel Flexible Reheat Combustor at Gas Turbine Relevant Operating Condition," Proceedings of ASME Turbo Expo., Glasgow, UK, June 14–18.
[21] Lückerath, R., 2015, "HTV-EB Robustes Hochtemperaturverbrennungssystem mit erweitertem Betriebsbereich," Schlussbericht, Teile I + II.
[22] Prathap, C., Galeazzo, F. C. C., Kasabov, P., Habisreuther, P., Zarzalis, N., Beck, C., Krebs, W., and Wegner, B., 2012, "Analysis of NO_x Formation in an Axially Staged Combustion System at Elevated Pressure Conditions," ASME J. Eng. Gas Turbines Power, **134**(3), p. 031507.
[23] Simcenter STAR-CCM+® Documentation User Guide Version 14.04, 2019, © Siemens PLM Software.
[24] Poinsot, T., and Vernante, D., 2005, *Theoretical and Numerical Combustion*, 2nd ed., ©2004 Book News, Inc., Portland, OR.
[25] Borghi, R., 1985, "On the Structure and Morphology of Turbulent Premixed Flames," *Recent Advances in the Aerospace Sciences*, Springer, Boston, MA, pp. 117–138.
[26] Genova, T., Otero, M., and Ahmed, K. A., 2020, "Partial Premixing Effects on the Reacting Jet of a High Pressure Axially Staged Combustor," J. Eng. Gas Turbines Power.
[27] Nori, V. N., and Seitzman, J. M., 2009, "CH* Chemiluminescence Modeling for Combustion Diagnostics," Proc. Combust. Inst., **32**(1), pp. 895–903.
[28] Yan, W., Wang, C., and Guo, J., 2012, "One Extended OTSU Flame Image Recognition Method Using RGBL and Stripe Segmentation," Appl. Mech. Mater., **121–126**, pp. 2141–2145.
[29] Combis, P., Cormont, P., Gallais, L., Hebert, D., Robin, L., and Rullier, J.-L., 2012, "Evaluation of the Fused Silica Thermal Conductivity by Comparing Infrared Thermometry Measurements With Two-Dimensional Simulations," Appl. Phys. Lett., **101**(21), p. 211908.
[30] Wray, K. L., and Connolly, T. J., 1959, "Thermal Conductivity of Clear Fused Silica at High Temperatures," J. Appl. Phys., **30**(11), pp. 1702–1705.
[31] Poinsot, T., Gicquel, L., Cuenot, B., Staffelbach, G., Vermorel, O., Wolf, P., Boileau, M., Colin, O., Veynante, D., Selle, L., Sensiau, C., Benoit, L., Gullaud, E., Berat, C., and Moureau, V., 2013, "Flame/Wall Interactions in Combustion Chambers," IMF Toulouse, CNRS and INPT, CERFACS Report.
[32] Harvey, P. D., 1982, *Engineering Properties of Steels*, American Society for Metals, Metals Park, OH.
[33] Peckner, D., Bernstein, I. M., and Peckner, D., 1977, *Handbook of Stainless Steels*, McGraw-Hill, New York. McGraw-Hill Book Company.
[34] Stiehl, B., Worbington, T., Miegel, A., Martin, S., Velez, C., and Ahmed, K., 2019, "Combustion and Emission Characteristics of a Lean Axial-Stage Combustor," Proceedings of ASME TurboExpo 2019., Phoenix, AZ, June 17–21.
[35] Stiehl, B., Worbington, T., Woodard, A., and Ahmed, K., 2020, "Numerical Simulation of an Axial-Staged Combustor at High Pressure," 2020 AIAA SciTech Forum and Exposition, Orlando, FL, Jan. 6–10.
[36] Stiehl, B., Otero, M., Genova, T., Worbington, T., Reyes, J., Ahmed, K., Martin, S., and Velez, C., 2021, "Simulation of Premixed and Partially Premixed Jet-in-Crossflow Flames at High-Pressure," ASME J. Eng. Gas Turbines Power., accepted manuscript.
[37] Genova, T., Otero, M., Stiehl, B., Reyes, J., Ahmed, K., and Martin, S., 2019, "Exploration of a Reacting Jet-in-Crossflow in a High-Pressure Axial Stage Combustor," AIAA Propulsion and Energy 2019 Forum, Indianapolis, IN, Aug. 19–22.
[38] Otero, M., Genova, T., Reyes, J., Stiehl, B., Ahmed, K., and Martin, S., 2019, "Characteristics of a Reacting Jet-in-Crossflow at Elevated Pressures," AIAA Propulsion and Energy 2019 Forum, Indianapolis, IN, Aug. 19–22.
[39] Smith, G. P., Golden, D. M., Frenklach, M., Moriarty, N. W., Eiteneer, B., Goldenberg, M., Bowman, C. T., Hanson, R. K., Song, S., Gardiner, Jr., W. C., Lissianski, V. V., and Qin, Z. "GRI-MECH 3.0," http://combustion.berkeley.edu/gri-mech/version30/text30.html
[40] Karalus, M., 2019, "Best Practices for RANS Combustion".
[41] Tominagaa, Y., and Stathopoulos, T., 2007, "Turbulent Schmidt Numbers for CFD Analysis With Various Types of Flowfield," Atmos. Environ., **41**(37), pp. 8091–8099.
[42] Loparo, Z., 2015, "Validation of CFD Models of a Second-Stage Combustion System Using STAR-CCM+," UTSR Internship Report University of Central Florida.
[43] Amirante, R., Distaso, E., Tamburrano, P., and Reitz, R. D., 2017, "Laminar Flame Speed Correlations for Methane, Ethane, Propane and Their Mixtures, and Natural Gas and Gasoline for Spark-Ignition Engine Simulations," Int. J. Engine Res., **18**(9), pp. 951–970.
[44] Bhargava, A., Kendrick, D. W., Colket, M. B., Sowa, W. M., Casleton, K. H., and Maloney, D. J., 2000, "Pressure Effect on NO_x and CO Emissions in Industrial Gas Turbines," Proceedings of ASME Turbo Expo 2000, Munich, Germany, May 8–11.